Sensitivity of Dynamic Mho Characteristic to PLL Parameters of Grid Following PV

Jayamohan, Meenu; Das, Sarasij ; Popov, Marjan

DOI
10.1109/INTELEC60315.2024.10679010

Publication date
2024

Document Version
Final published version

Published in
Proceedings of the 2024 IEEE International Communications Energy Conference (INTELEC)

Sensitivity of Dynamic Mho Characteristic to PLL Parameters of Grid Following PV

Meenu Jayamohan
Graduate Student Member, IEEE
Electrical Engineering
Indian Institute of Science
Bangalore, India
meenuj@iisc.ac.in

Sarasij Das
Senior Member, IEEE
Electrical Engineering
Indian Institute of Science
Bangalore, India
sarasij@iisc.ac.in

Marjan Popov
Fellow, IEEE
Faculty of EEMCS
Delft University of Technology
Delft, The Netherlands
M.Popov@tudelft.nl

2024 IEEE International Communications Energy Conference (INTELEC) | 979-8-3503-7057-7/24/$31.00 ©2024 IEEE | DOI: 10.1109/INTELEC60315.2024.10679010

***Abstract*—The restructuring of the power system by replacing Synchronous Generators (SGs) with Inverter-Based Resources (IBRs) has resulted in a drastic change in power system dynamics. Positive Sequence Memory Polarized (PSMP) mho elements have been used to ensure the reliable operation of mho relays during close-in bolted faults. The use of memory voltage for polarization of the mho element causes dynamic expansion of the mho characteristics. In an SG-only system, the memory polarization-induced dynamic expansion of these mho characteristics helps to increase the resistive reach. However, as the integration of IBRs increases, the dynamic mho expansion will be affected due to the different fault characteristics of IBRs. Most IBRs currently integrated into the power system are Grid-Following (GFOL) type, which uses Phase-Locked Loops (PLL) for synchronization. The variations in control parameters and bandwidths of the PLLs used in the GFOL IBRs may also affect the dynamic mho expansion. The studies presented in this paper demonstrate the impact of different types of PLLs and their control parameters on the dynamic expansion of PSMP mho relays. For this analysis, a modified IEEE-39 bus system with a GFOL Photovoltaic (PV) generator is used. The PVs have Voltage Support (VS), Low Voltage Ride-Through (LVRT)/ High Voltage Ride-Through (HVRT) features and comply with IEEE 2800-2022 standard.**

***Index Terms*—Dynamic mho expansion, Memory polarization, PV generator**

I. Introduction

The dynamics of the bulk power system have drastically changed as a result of the increased integration of Inverter-Based Resources (IBRs) like Photovoltaic (PV) generators and Wind Turbine Generators (WTGs). IBRs are interfaced with the grid using power electronic converters. Of the Grid Forming (GFM) and Grid Following (GFOL) converters in use, GFOL has been the most widely utilized. GFOL converters utilize Phase-Locked Loops (PLL) for synchronization. Once IBRs were incorporated into the utility grid, PLL usage significantly increased [1]. The converter controls govern the transient behavior of IBR systems, in contrast to Synchronous Generators (SGs). The impact of PLLs on transient stability, harmonic stability, and small signal stability in IBR-integrated systems has been undergoing a lot of research [2], [3].

The introduction of IBRs has significantly reduced the fault current produced as the short circuit current is limited by the power electronic components in the system. As a result, the existing protection schemes used for the conventional system may not work properly with the penetration of IBRs. One of the most widely used protection strategies for transmission lines is distance protection. The impact of IBRs on distance protection has been evaluated and analyzed in [4] - [6]. An adaptive protection scheme for a quadrilateral relay in lines connecting IBR plants using local data is proposed in [7]. Reference [8] proposes an adaptive distance relay scheme that is robust to fault resistance and adapts to different grid codes by adjusting its operation zone to improve fault detection and protection for lines connected to PV power plants. Again, for a quadrilateral relay, [9] has proposed a non-unit protection scheme for parallel lines connecting PV plants.

Mho relays are typically employed for the distance protection of transmission lines. Memory polarisation technique is frequently used for the protection of transmission lines employing mho elements to identify close-in faults [10]. The magnitude of the voltage falls almost to zero for close-in faults, which may cause the self-polarized mho element to fail. Memory voltage is used as the polarizing quantity in a Positive Sequence Memory Polarized (PSMP) mho relay. This is the weighted sum of positive sequence components of voltage during pre-fault and fault conditions. These memory polarization elements operate under the fundamental premise that, in the event of a fault, only the measured voltage amplitude changes quickly, whilst the change of its phase angle and frequency is negligible [11]. Additionally, it assumes that the additional resistive reach can be precisely estimated because the source impedance amplitude behind the relay is constant and predictable [8], [10]. This is true for a system with only SGs. However, this presumption may not be accurate for systems with IBRs. It is possible that the phase angle might not stay close to its pre-fault value [10]. Possible adverse effects of Wind Parks (WP) on memory polarized distance and directional elements have been discussed in [12]. It investigates the unpredictability of dynamic mho characteristics concerning wind speed, system strength, number of WTG units in operation, and choice of polarization. Reference [12] studies the impacts of IBR on the distance and directional elements that are memory polarized when the source behind the relay is either SG, Doubly Fed Induction Generator (DFIG)-based WP, or Full-Scale Converter (FSC)-based WP. The studies broadly compare self-polarized, cross-polarized, and PSMP mho circles under the above-mentioned scenarios. It does not focus on the effects of various control schemes of FSC-based IBRs. A novel offset-mho characteristic for memory polarized relay has been developed in [13]. The impacts of PQ control-based PV generation on PSMP mho relays are presented in [14]. Therein, the behavior of PSMP mho relays for a transmission system with PV generators is analyzed. It has also analyzed the PSMP mho element concerning pre-fault steady state operating point, changing weights, and behavior of converter control. Reference [15] studies the effects of $V_{dc}Q$ control of GFOL PV generation on PSMP mho relays. However, references [12] - [15] do not take into account the IEEE 2800 standard [16]. The benefits of the IEEE 2800 standard on various transmission line distance and directional protection functions are discussed in detail in [17]. Also, references [4] - [9], [12] - [15], and [17] do not study the impacts of PLL parameters on dynamic mho characteristics. The following summarizes the shortcomings of the existing research on the PSMP mho relays in the presence of IBRs.

- The impact of varying PLL parameters on the dynamic expansion of PSMP mho relays considering IEEE 2800-2022 standard [16] has not attracted much attention.
- Study on the impacts of different types of PLLs on dynamic mho characteristics is limited.

The analysis of dynamic mho expansion for PSMP mho relays in a transmission system with GFOL PV generation is presented in this paper. The system includes Low Voltage Ride-Through (LVRT)/ High Voltage Ride-Through (HVRT) and Voltage Support (VS) capability and adheres to the IEEE 2800-2022 standard. The major contributions of this work are,

- The dynamic mho expansion for PSMP mho relays has been analyzed by varying the PLL parameters, K_p and K_i, for a GFOL PV integrated system.
- The performance of PSMP mho characteristics has been studied for different types of PLL-Synchronous Reference Frame PLL with Low Pass Filter (LSRF PLL) and Dual Second-Order Generalized Integrator (DSOGI) PLL.
- The diameter of the maximum expansion of dynamic PSMP mho element, d_{max}, and the angle of the corresponding memory vector, θ_m, have been analyzed for varying PLL parameters and types of PLL.

II. Investigated PLLs

Power systems and power electronics have employed PLLs for different purposes, such as control and synchronization. When IBRs were added to the utility grid, PLL usage significantly increased. The task of PLL is to maintain the output frequency and the input reference signal frequency synchronized using phase comparison [1]. The three main parts of a PLL are a Phase Detector (PD), Loop Filter (LF), and Voltage Controlled Oscillator (VCO). The main distinction between different types of PLL is the design of the PD block. The VCO is described as an integrator, and the LF as a Proportional-Integral (PI) controller. In Fig. 1 and Fig. 2, superscript '+' represents positive sequence component. Subscripts 'd', 'q', 'α' and 'β' denotes d-axis, q-axis, α-axis, and β-axis components respectively. Filtered components are represented by subscript 'f.' The voltage at the Reference Point of Applicability (RPA) is v_{abc}, and the nominal frequency, ω_{nom}, is $2\pi 60$ rad/s.

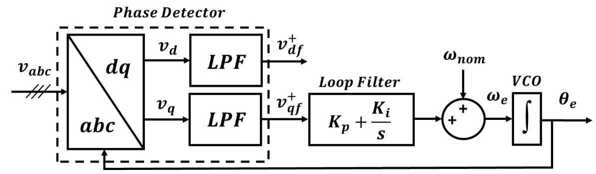

Fig. 1. Basic structure of LSRF PLL

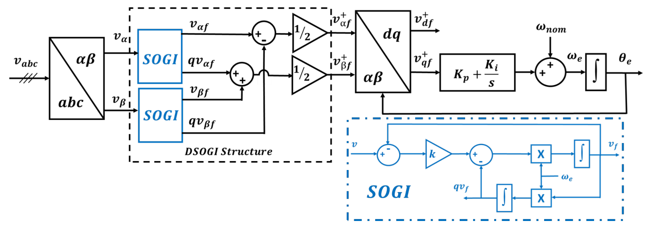

Fig. 2. Basic structure of DSOGI PLL

A. LSRF PLL

As it is the simplest to implement, the Synchronous Reference Frame PLL (SRF PLL) is the most often used PLL. For optimal grid circumstances, it produces good results. However, when the grid voltage is out of balance or tainted with harmonics, it cannot be effective [1]. Adding Low Pass Filters (LPF) is one way to address the previously described problem. An SRF PLL with extra LPF is described as an "LSRF PLL," as depicted in Fig. 1. A first-order filter with a cut-off frequency of ω_{LPF}, 44.0844 Hz, has been developed as the LPF for LSRF PLL [18]. The following is the small signal model of PLL's open loop transfer function:

$$G_{opl}(s) = \left(\frac{\omega_{LPF}}{s+\omega_{LPF}}\right) K_p \left(\frac{s+K_i/K_p}{s}\right)\frac{1}{s} \qquad (1)$$

B. DSOGI PLL

DSOGI PLL facilitates identifying the positive-sequence component at the fundamental frequency of the utility voltage under unbalanced and corrupted scenarios. It is a dual second-order generalized integrator-based PLL operating on the instantaneous symmetrical components theory [1]. DSOGI PLL's fundamental architecture is illustrated in Fig. 2. For DSOGI PLL, the damping factor of SOGI block, k $= 2\omega_{LPF}/\omega_{nom}$ [18]. Reference [18] provides a detailed design that takes into account the transient response, stability margin, and disturbance rejection. G_{opl} is also same as in (1). LSRF PLL and DSOGI PLL are used in this paper to study the effects of varying PLL parameters.

III. Test System for the Study

The IEEE 39-bus system operating at 345 kV and 60 Hz is modified and modeled in PSCAD to ensure that the fault

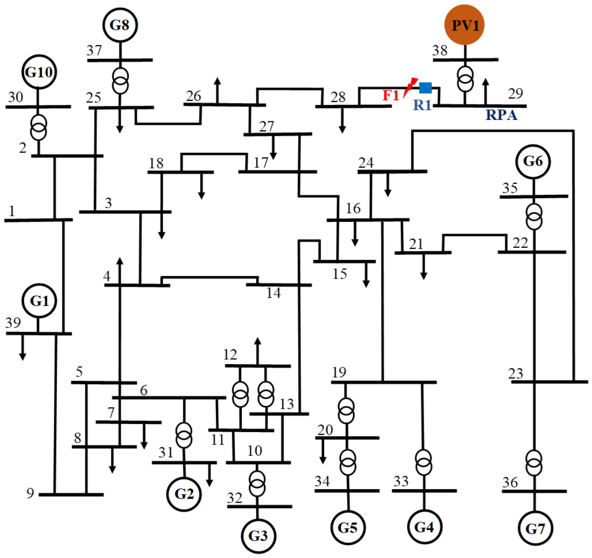

Fig. 3. Modified IEEE-39 bus transmission system with PV integration

current seen by the relay $R1$ is fully contributed by the PV generator $PV1$, as depicted in Fig.3. The PV generator $PV1$, connected to bus 38, is an 870.5 MVA, 33 kV, GFOL PV generator, modeled using an average model [19]. This work focuses on phasor domain analysis, specifically the fundamental 60 Hz component observed by the relay. The transient behavior at switching frequencies is neglected as the main interest lies in the power system performance at the fundamental frequency, not the harmonic content near switching [20], [21]. Hence, the average model adequately represents the PV in this work. The system configuration is illustrated in Fig.3, with $R1$ located on line 28-29. The PV inverter is configured to supply reactive current (or power) during faults, prioritizing reactive power called Q-priority. The PV has LVRT/HVRT and voltage support (VS) capabilities as specified in [16]. The LVRT/HVRT characteristics are shown in Fig.5. Constant solar irradiation is assumed throughout the analysis.

The inverter operates in the dq reference frame, with transformations between abc and dq aligned with the PLL angle θ_e. The d-axis controls manage real power output (P_{out}), while the q-axis controls handle reactive power output (Q_{out}) of $PV1$. Under steady-state operating conditions, the terminal voltage at the Reference Point of Applicability (RPA) stays between 0.9 p.u. and 1.05 p.u. The Maximum Power Point Tracker (MPPT) output, P_{set}, is used as P_{ref}, and Q_{ref} is set to Q_{set}=0.3287P_{set}. When the VS functionality is active, it provides reactive power support as required by the grid code. If voltage limits are exceeded, equations (2)-(4) are applied to determine the reference values for real and reactive power. The VS functionality supplies reactive power in proportion to the change in voltage corresponding to the value of K [19].

$$Q_{vs} = K(V_{nominal} - V_{rpa}) \tag{2}$$

where, Q_{vs} is the reactive power provided by the VS, V_{rpa} is the terminal voltage at RPA and $V_{nominal}$ is the nominal

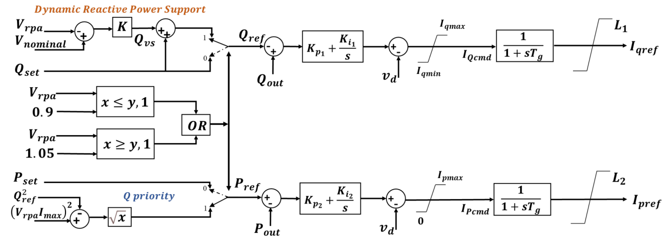

Fig. 4. Control logic for the average model of PV generator

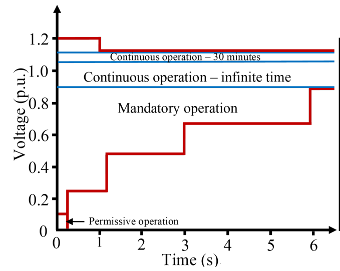

Voltage at RPA (p.u.)	Operating mode/response	Minimum ride-through time (s)
V>1.2	May ride-through / trip	NA
V>1.1	Mandatory operation	1
V>1.05	Continuous operation	1800
V<0.9	Mandatory operation	6
V<0.7	Mandatory operation	3
V<0.5	Mandatory operation	1.2
V<0.25	Mandatory operation	0.32
V<0.1	Permissive operation	0.32

Fig. 5. Low Voltage/High Voltage Ride-Through characteristics

voltage at the RPA. K is considered to be two here and can range from 1 to 10 [22]. When VS gets activated:

$$Q_{ref} = Q_{vs} + 0.3287P_{set} \tag{3}$$

$$P_{ref} = \sqrt{(V_{rpa}I_{max})^2 - Q_{ref}^2} \tag{4}$$

where, to restrict the inverter's output current, I_{max} is set to 1.2 p.u. and all the quantities in the above equations are in per unit. The Q_{ref} is compared to the Q_{out}, and the error signal is then fed through the PI controller to generate the q-axis current command, I_{Qcmd}. Similarly, P_{ref} is compared to P_{out}, and the error is processed by a PI controller to obtain the d-axis current command, I_{Pcmd}. These current command signals are limited as specified in [23]. Subsequently, low-pass filters with a time constant of T_g=0.02 s are applied to I_{Qcmd} and I_{Pcmd} to obtain the d-axis and q-axis current references, I_{pref} and I_{qref}, respectively. As shown in Fig. 4, these current references are further limited by values L_1 and L_2. The PI blocks used in the PV control are K_{p1}=K_{p2}=0.05 and K_{i1}=K_{i2}=1.

IV. Dynamic Mho Characteristics

The polarizing and operating quantities for a mho relay element are Z_{pol} and Z_{op}, respectively. The reach setting of the relay can be defined as the impedance of the protected portion of the transmission line, Z_r. The apparent impedance seen by the relay, Z_{app}, is calculated by the mho element from the system currents and voltages, which acts as the polarizing quantity in a self-polarized mho relay. The operating quantity, Z_{op}, of the mho element is Z_{op}= Z_r-Z_{app}. The self-polarized mho element is explained in detail in [14], [15]. Memory polarization has then been developed due to the drawbacks of a self-polarized mho relay during close-in faults.

Traditional self-polarized mho relays utilize the faulty phase voltage for polarization. However, during close-in faults, the

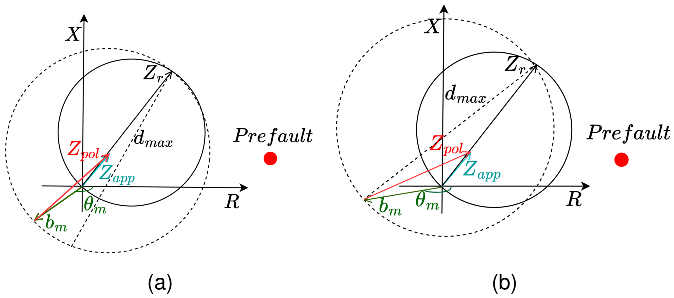

Fig. 6. Dynamic mho expansion for (a) SG-only system (b) system with GFOL PV generation

voltage of the faulty phase will be near zero or zero. This voltage can be unreliable as it might not be sufficient to polarize the mho element, leading to inaccurate relay operation. PSMP mho relays address this limitation by employing the positive sequence pre-fault voltage for polarization. This pre-fault voltage is stored as a "memory voltage" through a dedicated memory filter. Over time, the memory voltage progressively converges towards the actual fault voltage. Hence, PSMP mho relays are widely used for transmission line protection. The Z_{pol} in a PSMP mho relay is calculated from the fault current, I_f, and positive sequence memory voltage, $V_{f,m}^{+}$. The memory voltage for the i^{th} protection pass is defined as,

$$V_{f,m}^{+}(i) = \omega . V_f^{+}(i) + (1-\omega) . V_{f,m}^{+}(i-j) \quad (5)$$

where $V_{f,m}^{+}$ represents the positive sequence memory voltage phasor, V_f^{+} represents the positive sequence faulty phase voltage phasor, and ω represents the weight factor. In this study, ω is set as 0.5; however, it can have values between 0 and 1. The memory voltage for the i^{th} protection pass is the voltage from the $i-j$ protection pass. The dynamic mho expansion will result from this polarizing memory voltage. Fig. 6a illustrates the dynamic PSMP mho expansion for a three-phase to ground fault occurring on an SG-only system. The memory vector is shown by the vector b_m, and its angle with respect to the positive resistance axis (R-axis) is indicated by θ_m. For a three-phase to ground fault, the polarizing impedance, Z_{pol}, and apparent impedance, Z_{app}, are computed as,

$$Z_{app}(i) = \frac{V_f(i)}{I_f(i)}; \qquad Z_{pol}(i) = \frac{V_{f,m}^{+}(i)}{I_f(i)} \quad (6)$$

The memory vector, b_m and the diameter of the dynamic mho circle, d_m are calculated from (6) as

$$b_m(i) = Z_{app}(i) - Z_{pol}(i); \quad d_m(i) = |Z_r(i) - b_m(i)| \quad (7)$$

The maximum value of $d_m(i)$ is represented as d_{max}, which is the maximum dynamic PSMP mho expansion. The memory vector corresponding to d_{max} is b_m, and the angle of b_m with the positive R-axis is represented as θ_m. The dynamic expansion of the mho circle is governed by the memory vectors. This dynamic expansion has been shown to provide greater resistive coverage for the mho element. The memory voltage, which dynamically expands the mho circle, enhances its ability to detect faults with resistive components. The memory vector, which is the difference between the polarizing impedance and the apparent impedance, controls this expansion. The degree of resistive coverage is mostly dependent on the angle of the memory vector with respect to the positive R-axis. The steady-state operating point before fault occurrence is represented by "Prefault" in Figs. 6a and 6b. For an SG-only system, as shown in Fig. 6a, low pre-fault voltage and large fault current result in a low magnitude of Z_{pol}. As a result, b_m, which is a product of Z_{pol} and Z_{app}, becomes very small. However, the b_m is significantly longer, and its angle, θ_m, is larger for a PV-integrated system from Fig. 6b than for an SG-only system, which decreases its resistive reach [15]. In this paper, a higher value of θ_m indicates that the memory vector b_m is moving further away from the positive R-axis or the negative X-axis. Conversely, a lower value of θ_m means b_m is getting closer to the positive R-axis or the negative X-axis.

V. Results

A three-phase to ground fault, $F1$, is generated for a duration of 0.07 sec on line 28-29 at a distance of 2% from bus 29, as shown in Fig. 1. The observations are presented for fault resistance $R_f = 0\ \Omega$. PSCAD is used for simulations, and the voltages and currents are calculated at a high rate of 3.84 kHz to obtain 64 samples/cycle. Additional calculations have been performed in MATLAB using PSCAD fault data. Eight protection passes are considered in a cycle. The prior two cycle's memory voltage is obtained by setting the value j in (5) to 16. The PSMP function gets activated when the faulty phase voltage goes below a threshold, which is considered as 0.4 times the pre-fault phase voltage. The maximum expansion of the dynamic mho characteristic of the PSMP mho element is analyzed by varying the PLL parameters-K_p and K_i. A closed loop bandwidth range from 2.36 Hz to 18 Hz is considered a standard PLL bandwidth for power system investigations [2]. Trends observed in the diameter of the maximum expansion of the dynamic PSMP mho circle, d_{max}, and its corresponding memory voltage angle, θ_m, in the covered bandwidth range are analyzed.

A. LSRF PLL

1) K_p constant: In this case, K_i varies from 20 to 1050, whereas K_p remains fixed at 50. This combination of K_p and K_i covers a bandwidth range of 7.8 Hz to 11 Hz. No particular trend is observed for d_{max} and θ_m as the bandwidth increases. The maximum expansions of dynamic PSMP mho circle for a constant K_p value, along with self-polarized mho characteristics, are shown in Fig. 7a.

2) K_i constant: In this case, K_p varies from 5 to 100, whereas K_i remains fixed at 200, covering a bandwidth range of 3.28 Hz to 18 Hz. No particular trend is observed for d_{max} and θ_m when the bandwidth varies. The maximum expansions of dynamic PSMP mho circle for a constant K_i value, along with self-polarized mho characteristics, are shown in Fig. 7b.

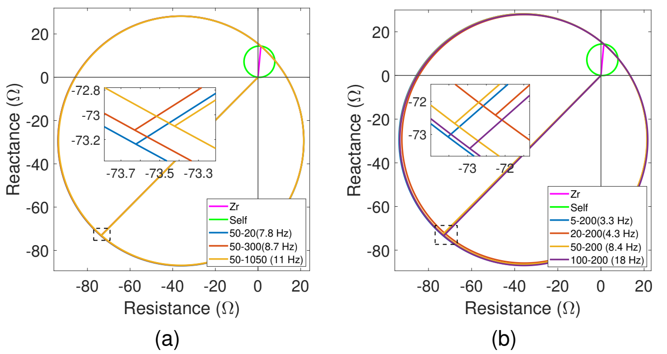

Fig. 7. Maximum dynamic mho expansion seen by $R1$ for LSRF PLL when (a) K_p=50 (b) K_i=200

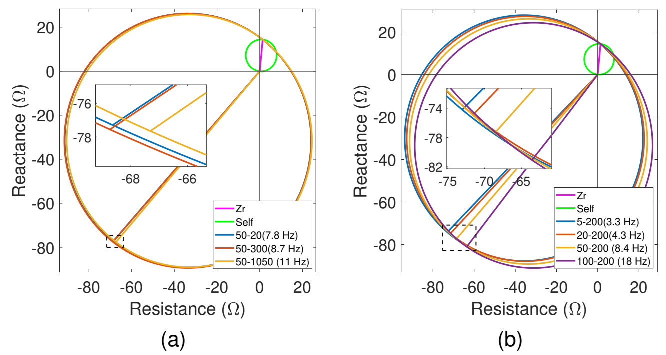

Fig. 9. Maximum dynamic mho expansion seen by $R1$ for DSOGI PLL when (a) K_p=50 (b) K_i=200

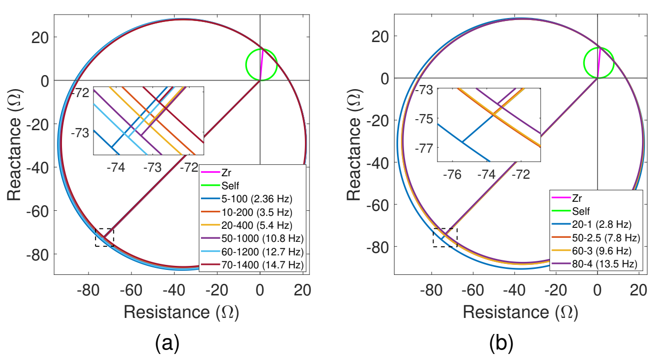

Fig. 8. Maximum dynamic mho expansion seen by $R1$ for LSRF PLL when (a) K_i/K_p=20 (b) K_i/K_p=0.05

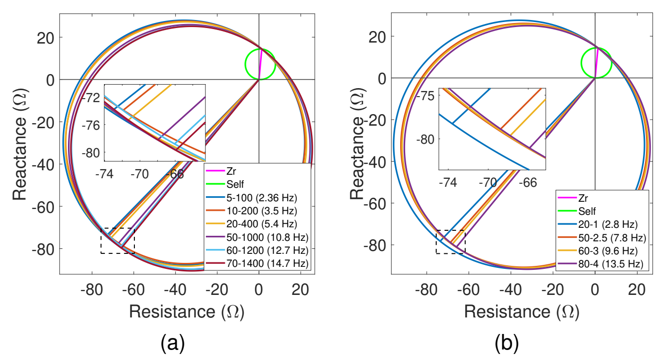

Fig. 10. Maximum dynamic mho expansion seen by $R1$ for DSOGI PLL when (a) K_i/K_p=20 (b) K_i/K_p=0.05

The values of these parameters are very close to each other as the bandwidth varies to make any specific inferences.

3) K_i/K_p high: Here, the K_i/K_p value is set as 20. A combination of K_p and K_i is employed, with the bandwidth spanning from 3.5 Hz to 14.7 Hz. Here also, no particular trend is observed for d_{max} and θ_m, as shown in Fig. 8a. The values of d_{max} and θ_m do not experience significant changes with varying bandwidth values, and they stay close to each other, where a trend cannot be established.

4) K_i/K_p low: K_i/K_p value is set as 0.05 in this case. A bandwidth range of 2.8 Hz to 13.5 Hz is covered by adjusting the K_p and K_i values. Here, as shown in Fig. 8b, as the bandwidth increases, no particular trend is observed for d_{max} and θ_m. The d_{max} and θ_m values are very close to each other during the bandwidth variation to make any specific inferences.

Hence, it has been observed that for LSRF PLL, a specific trend in the variation of d_{max} or θ_m cannot be established with the variation in PLL parameters. In all the above cases considered, the d_{max} and θ_m have been observed to stay close to each other, with no particular trend, with the variation in PLL bandwidth.

B. DSOGI PLL

All the cases of varying PLL parameters considered for LSRF PLL are also considered for DSOGI PLL. It has been observed that the difference in d_{max} and θ_m, for varying PLL parameters, is more prominent for DSOGI PLL than that for LSRF PLL.

1) K_p constant: For this case, similar to LSRF, no specific trend has been observed for d_{max}. However, θ_m decreases as the bandwidth increases, and the difference is more prominent than LSRF PLL. The comparative analysis for cases with different bandwidths of LSRF and DSOGI PLL shows that d_{max} for DSOGI PLL is higher than that for LSRF PLL while θ_m for DSOGI is lower (closer to positive R-axis) than that for LSRF PLL. However, the difference in d_{max} between DSOGI and LSRF PLL is very small. The decrease in θ_m improves the resistive reach for DSOGI PLL compared to LSRF PLL. Furthermore, it has been noted that when the bandwidth increases, the difference in θ_m for the corresponding cases between DSOGI and LSRF PLL increases.

2) K_i constant: Here also, no specific trend is observed for d_{max}. However, as the bandwidth increases, θ_m decreases. It has also been observed that the difference in θ_m as bandwidth increases is more prominent than that for LSRF PLL. Besides, observations similar to those in the previous case are observed in the comparison of the corresponding cases of bandwidths for LSRF and DSOGI PLL. It has also been observed that d_{max} for DSOGI PLL is higher, and θ_m for DSOGI is lower than that for LSRF PLL.

3) K_i/K_p high: Here, as the bandwidth increases θ_m decreases. No specific trend is observed for d_{max}. For the corresponding bandwidth cases, results are the same as before.

4) K_i/K_p low: Here, no specific trend is observed for d_{max}. However, as the bandwidth increases, θ_m decreases as in all the previous cases of DSOGI. The comparison of corresponding cases of bandwidth of LSRF and DSOGI PLL yields similar observations as the previous cases of DSOGI.

C. Observations

- No particular trend in d_{max} or θ_m have been observed with LSRF PLL as bandwidth is varied.
- For DSOGI PLL, for all the cases of varying PLL parameters, θ_m is found to decrease (move closer to positive R-axis) as bandwidth increases. But no particular trend has been observed for d_{max}.
- On comparing results for LSRF and DSOGI PLLs for corresponding bandwidths, d_{max} is slightly higher and θ_m is lower for DSOGI PLL compared to LSRF PLL.
- The reduced θ_m for DSOGI PLL compared to LSRF PLL for a given bandwidth improves the resistive reach for DSOGI PLL during memory polarization.
- It has also been observed that the difference in θ_m for corresponding cases between DSOGI and LSRF PLL increases as bandwidth increases.

VI. CONCLUSION

This paper presents new findings on the impacts of PLLs of a GFOL PV generator on dynamic mho expansion. The impacts of LSRF and DSOGI PLLs on the diameter of the maximum expansion of the dynamic mho circle, d_{max}, and the angle made by the memory vector, θ_m, while changing the bandwidth of the PLLs, are analyzed. A comparison is made between LSRF and DSOGI PLLs for θ_m and d_{max}. It has been observed that the PLL bandwidths impact the dynamic mho expansion depending on the PLL types. For LSRF PLL, the observed effect is not that significant. However, DSOGI PLL is found to be more sensitive to changes in bandwidth. It has been observed that the DSOGI offers better resistive reach during memory polarization compared to LSRF as its d_{max} is higher and θ_m is smaller (closer to positive R-axis) than the LSRF PLL for the same bandwidths. So, the impact of PLL parameters on dynamic mho characteristics should be carefully studied when DSOGI PLL is used.

ACKNOWLEDGMENT

This research has been partly conducted using the ERIGrid 2.0 Research Infrastructure and is part of a project that has received funding from the European Union's Horizon 2020 Research and Innovation Programme under Grant Agreement No. 870620, to conduct research at Delft University of Technology, the Netherlands. This work has also been partly funded by the IISc-TU Delft Joint Seed Fund 2022.

REFERENCES

[1] S. Golestan, J. M. Guerrero, and J. C. Vasquez, "Three-Phase PLLs: A Review of Recent Advances," *IEEE Trans. Power Electron.*, vol. 32, no. 3, pp. 1894-1907, March 2017.

[2] J. Liu et al., "Impact of Power Grid Strength and PLL Parameters on Stability of Grid-Connected DFIG Wind Farm," *IEEE Trans. Sustain. Energy*, vol. 11, no. 1, pp. 545-557, Jan. 2020.

[3] I. R. S. Priyamvada and S. Das, "Impact of PLL on Harmonic Stability of Renewable Dominated Power System: Modeling and Analysis," 2018 IEEE International Conference on Power Electronics, Drives and Energy Systems (PEDES), Chennai, India, 2018, pp. 1-6.

[4] J. J. Chavez, M. Popov, D. López, S.Azizi, and V. Terzija, "S-Transform based Fault Detection Algorithm for Enhancing Distance Protection Performance," *Int. J. Electr. Power Energy Syst.*, Vol. 130, 2021.

[5] X. Zhang, M. Radwan, and S. Pirooz Azad, "Modified Distance Protection of Transmission Lines Originating from DFIG-Based WPPs by Considering the Impact of Fault-Induced Rotor Frequency and LVRT Requirements," *Int. J. Electr. Power Energy Syst.*, Vol. 147, 2023.

[6] Kasztenny, B., "Distance Elements for Line Protection Applications Near Unconventional Sources.", SEL Inc., Nov. 2022.

[7] S. Paladhi and A. K. Pradhan, "Adaptive Distance Protection for Lines Connecting Converter-Interfaced Renewable Plants," *IEEE J. Emerg. Selec. Topics Power Electron.*, vol. 9, no. 6, pp. 7088–7098, Dec. 2021.

[8] Y. Liang, W. Li and W. Zha, "Adaptive Mho Characteristic-Based Distance Protection for Lines Emanating From Photovoltaic Power Plants Under Unbalanced Faults," *IEEE Syst. J.*, vol. 15, no. 3, pp. 3506-3516, Sept. 2021.

[9] A. Chowdhury, S. Paladhi and A. K. Pradhan, "Nonunit Protection of Parallel Lines Connecting Solar Photovoltaic Plants," *IEEE Syst. J.*, vol. 17, no. 2, pp. 2961-2970, June 2023.

[10] D. D. Fentie, "Understanding the Dynamic Mho Distance Characteristic," in 2016 69th Annual Conference for Protective Relay Engineers (CPRE), IEEE, 2016, pp. 1–15.

[11] "Impact of Inverter Based Generation on Bulk Power System Dynamics and Short-Circuit Performance," IEEE Power and Energy Society, PES-TR68, Tech. Rep., 2018.

[12] A. Haddadi, M. Zhao, I. Kocar, E. Farantatos, and F. Martinez, "Impact of Inverter-Based Resources on Memory-Polarized Distance and Directional Protective Relay Elements," 2020 52nd North American Power Symposium (NAPS), Tempe, AZ, USA, 2021.

[13] E. Sorrentino, J. Melián, and V. De Andrade, "A Novel Method to Obtain the Offset Mho Characteristic of Memory-Polarized and Cross-Polarized Distance Functions of Protective Relays from Experimental Measurements," *Electric Power Syst. Res.*, Vol. 216, 2023.

[14] A. Radhakrishnan, I. R. S. Priyamvada and S. Das, "Impact of P – Q Control based PV Generator on Memory-Polarized Mho Relay," 2022 International Conference on Smart Energy Systems and Technologies (SEST), 2022, pp. 1-6.

[15] A. Radhakrishnan, A. Ghosh, I. R. Sai Priyamvada and S. Das, "Performance of Memory-Polarized Distance Relay in Presence of PV Generator with VdC-Q Control," IEEE Energy Conversion Congress and Exposition (ECCE), Detroit, MI, USA, 2022, pp. 1-8.

[16] "IEEE Standard for Interconnection and Interoperability of Inverter-Based Resources (IBRs) Interconnecting with Associated Transmission Electric Power Systems," in IEEE Std 2800-2022.

[17] M. J. B. B. Davi, M. Oleskovicz, F. V. Lopes, " Study on IEEE 2800-2022 Standard Benefits for Transmission Line Protection in the Presence of Inverter-Based Resources," *Electric Power Syst. Res.*, Vol. 220, 2023.

[18] S. Golestan, M. Monfared and F. D. Freijedo, "Design-Oriented Study of Advanced Synchronous Reference Frame Phase-Locked Loops," *IEEE Trans. Power Electron.*, vol. 28, no. 2, pp. 765-778, Feb. 2013.

[19] M. Jayamohan, S. Das and S. Brahma, "Impedance Trajectories during Stable and Unstable Power Swings in Presence of PQ Control based PV Generations," 2023 IEEE Power and Energy Society General Meeting (PESGM), Orlando, FL, USA, 2023, pp. 1-5.

[20] U. Karaagac et al., "A Generic EMT-Type Model for Wind Parks With Permanent Magnet Synchronous Generator Full Size Converter Wind Turbines," *IEEE Power Energy Technol. Syst. J.*, vol. 6, no. 3, pp. 131-141, Sept. 2019.

[21] R. T. Elliott, A. Ellis, P. Pourbeik, J. J. Sanchez-Gasca, J. Senthil and J. Weber, "Generic Photovoltaic System Models for WECC - A Status Report," 2015 IEEE PES General Meeting (PESGM), Denver, CO, USA, Jul. 2015, pp. 1–5.

[22] P. Adhikari, S. Brahma, and P. H. Gadde, "Source-Agnostic Time-Domain Distance Relay," *IEEE Trans. Power Del.*, vol. 37, no. 5, pp. 3620-3629, Oct. 2022.

[23] M. Jayamohan, S. Das and S. Brahma, "Impact of Dynamic Voltage Support and Active Power Recovery Rate on Power Swing Blocking Protection in Presence of Grid-Following PV," 2024 Kansas Power and Energy Conference (KPEC), Manhattan, USA, 2024.